Available online at www.sciencedirect.com
ScienceDirect
Energy Reports 9 (2023) 806–818
www.elsevier.com/locate/egyr

2022 International Conference on Frontiers of Energy and Environment Engineering, CFEEE 2022, 16–18 December, 2022, Beihai, China

Analytical DC-side stabilizing conditions for hybrid HVDC links based on dominant frequency model reduction

Jiapeng Li[a,b], Yujun Li[a,b,*], Minghao Wang[b], Shudan Wang[a], Zhao Xu[b], Guobing Song[a]
[a] *Xi'an Jiaotong University, No. 28 Xianning West Road, Xi'an 710049, China*
[b] *The Hong Kong Polytechnic University, No. 11 Yuk Choi Road, Kowloon 999077, Hong Kong*

Received 30 March 2023; accepted 10 April 2023
Available online 21 April 2023

Abstract

Incorporating the advantages of line commutated converters (LCCs) and voltage-source converters (VSCs), hybrid high voltage DC (HVDC) links have bright prospects in bulk power transmission. For this new technique, however, there is a risk of oscillatory instability in the DC link, and the mechanism behind the instability is still unclear. This paper derives analytical DC-side stabilizing conditions for hybrid HVDC links by using dominant frequency model reduction. The small-signal model of the LCC-VSC link is first truncated by reserving only the state variables highly relevant to the dominant mode so that the expression of the dominant oscillation frequency can be obtained. Dynamics of other state variables are reintroduced and then simplified while leaving their properties nearby the dominant frequency intact. Based on the reduced model, an analytical stability criterion is obtained, which reveals that the DC-side stability of hybrid HVDC links will deteriorate with reduced DC voltage operation, a heavy load, a small DC-link capacitor, slow inner loop dynamics, a small proportional and a large integral gain of the DC voltage regulator. In addition, simplified sufficient stabilizing conditions of hybrid HVDC links are further derived for control parameter design. Case studies validate the accuracy of dominant frequency model reduction and the derived stabilizing conditions.

Peer-review under responsibility of the scientific committee of the 2022 International Conference on Frontiers of Energy and Environment Engineering, CFEEE, 2022.

Keywords: Hybrid HVDC link; DC-side resonances; Analytical stabilizing conditions; Dominant mode; Model reduction

1. Introduction

Born in the 1960s, the line commutated converter (LCC) has gradually become the most widely used converter in high voltage DC (HVDC) projects for the low cost and large capacity [1]. However, the LCC has drawbacks of commutation failure risks when operating as an inverter and the inability to supply weak AC systems [2]. Recently, the voltage source converter (VSC) has become prevailing in DC power transmission. Due to the use of full-controlled insulated gate bipolar transistors (IGBTs) or gate turn-off (GTO) thyristors, the VSC distinguishes itself

* Corresponding author at: Xi'an Jiaotong University, No. 28 Xianning West Road, Xi'an 710049, China.
E-mail address: yujunlizju@xjtu.edu.cn (Y. Li).

https://doi.org/10.1016/j.egyr.2023.04.103

Peer-review under responsibility of the scientific committee of the 2022 International Conference on Frontiers of Energy and Environment Engineering, CFEEE, 2022.

with the decoupling control of active and reactive power, needlessness of AC system supports, and commutation failure elimination [3]. Despite these, the cost and power loss of VSC are relatively higher than those of the LCC. The hybrid HVDC transmission that employs the LCC based rectifier(s) and the VSC based inverter(s) was first proposed in 1992 to incorporate the advantages of the two types of converters [4]. For its wider applications in renewable resources integration, substantial researches have been done concerning the operation [5], control [6–9], and protection [10,11] of the hybrid HVDC system. However, few works concentrate on its small-signal stability, fundamentally hindering its broader applications.

To date, existing works mainly focus on the small-signal stability discrimination for hybrid HVDC links based on the classic modal analysis. The small-signal model of the hybrid LCC-VSC HVDC link is first established in [12]. Based on eigenvalue and participation factor analysis, it is unveiled that improper system parameters will cause oscillatory instability in the hybrid HVDC link. [13] reports the relationships between stability properties and controller parameters in hybrid HVDC systems by using the segmented LaGrange quadratic interpolation. The eigen analysis shows that the DC-side stability can be enhanced by choosing a large proportional gain or a small integral gain of the DC voltage regulator. In [14], the feasible region of DC voltage controller parameters is further determined based on stability analysis of hybrid HVDC systems. Nevertheless, the modal analysis relies on relatively complicated eigenvalue calculations, which fails to derive an analytical stability criterion based on key system parameters. As a result, repeated eigenvalue calculations are required once the system operating point or a controller parameter changes.

Complicated eigenvalues calculations can be avoided, provided that the analytical stability criterion of the system under study is obtained. In view of the complexity of the studied system, model reduction is critical to simplify the analysis. In singular perturbation theory (SPT), the original system is decomposed into reduced-order and boundary-layer subsystems [15]. The reduced-order subsystem expresses slow dynamics, while the fast dynamics impacts are regarded as boundary-layer corrections computed in separated time scales [16]. Despite the clear physical meaning of the reduction process, SPT may not be accurate enough to analyze the system properties within specified frequency bands. Selective modal analysis (SMA) is widely adopted in power system low-frequency oscillation analysis [17,18]. Unlike SPT, SMA can accurately retain the properties of selected modes after the reduction. Nevertheless, the reduced model is obtained via iterative numerical calculations, which must be regenerated once any system parameter varies. Balanced truncation theory (BRT) is another effective model reduction method with fairly high accuracy [19]. In this method, system state variables are reconstructed via matrix transformation such that the transformed controllability Grammian is diagonal and equals the observability Grammian, which is known as balanced realization [20]. Model reduction is then achieved by omitting those less controllable or observable state variables. Unfortunately, these reformed state variables lack clear physical meaning, resulting in poor interpretability of the reduced-order model.

Existing works on the small-signal stability of the hybrid HVDC system fail to establish mathematical relations between the stability properties and the influential factors, resulting in a relatively heavy computation burden for stability discrimination. In this paper, dominant frequency mode reduction is utilized to derive analytical stabilizing conditions for the hybrid LCC-VSC HVDC system under DC-side perturbations. Focusing on the properties nearby the dominant frequency, the proposed model reduction stands out for its good interpretability, analytic form, and high accuracy in expressing the dominant mode. An analytical stability criterion for hybrid HVDC links is further derived based on the reduced model, which well indicates that the system stability will deteriorate with reduced DC voltage operation, a heavy load, a small DC-link capacitor, slow inner loop dynamics, a small proportional and a large integral gain of the DC voltage regulator. The derived analytical stability criterion facilitates the online stability assessment and guides in designing the control parameters.

2. Modeling of the hybrid LCC-VSC HVDC link

2.1. System description

Fig. 1 depicts the typical topology of a hybrid two-terminal HVDC system, where one LCC-based rectifier and one VSC-based inverter are connected by a DC transmission line. The DC-link voltage of the rectifier and the inverter are marked as u_{dcr} and u_{dci}, respectively. The DC-link current is i_{dc}, whose positive direction is defined as from the rectifier to the inverter. To suppress DC-link current harmonics and limit current surges during DC faults, smoothing reactors L_d and L_t are implemented. The transmitted active power through the VSC-based inverter is denoted by P_c. Normally, the LCC-based rectifier regulates the DC-link current, while the VSC-based inverter controls the DC-link voltage.

Fig. 1. Schematic of the two-terminal hybrid HVDC system.

2.2. Dynamics of the hybrid LCC-VSC HVDC system

(1) LCC-based rectifier: Fig. 2 shows the topology and the equivalent circuit of the LCC-based rectifier. V_o is the ideal no-load voltage of the LCC and $V_o = 3\sqrt{2}E/\pi$, in which E is the root-mean-square line voltage of the LCC-connected AC source. α is the firing angle of the LCC. d_γ is the equivalent commutation resistance and $d_\gamma = 3\omega_s L_\gamma/\pi$, in which ω_s is the frequency of the LCC-connected AC source and L_γ is the inductance of the commutation reactor. The dynamics of the LCC-based rectifier can be described as,

$$u_{dcr} = V_o \cos\alpha - d_\gamma i_{dc} \tag{1}$$

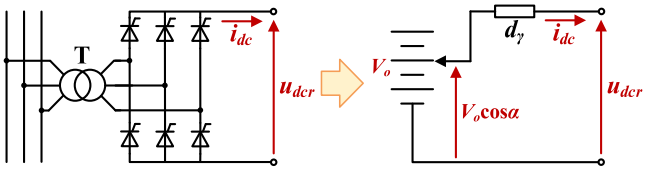

Fig. 2. Topology and equivalent circuit of the LCC-based rectifier.

As shown in Fig. 3, the LCC regulates the DC-link current by tuning the firing angle α with a proportional–integral (PI) controller, which is expressed as,

$$\alpha = \pi - K_{Pc}\left(i_{dc}^{ref} - i_{dc}\right) - x_c, \quad x_c = K_{Ic}\int\left(i_{dc}^{ref} - i_{dc}\right)\mathrm{d}t \tag{2}$$

where i_{dc}^{ref} is the reference DC-link current. K_{Pc} and K_{Ic} are the proportional and integral (PI) gains of the constant current controller. x_c is the integral part of the PI current controller. The PI controller is assumed not to saturate under DC-side perturbations.

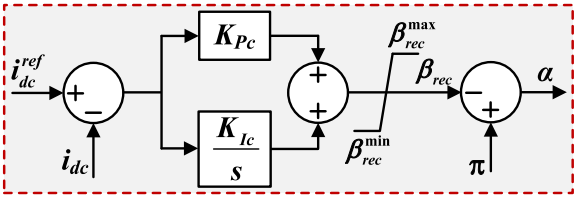

Fig. 3. DC current control of the LCC.

To solely and fully investigate the DC-side stability of hybrid HVDC links, the AC system supplying the LCC is assumed to be ideal, implying the dynamics of the PLL of the LCC-based rectifier are neglected.

(2) VSC-based inverter: Fig. 4 shows the equivalent circuit of the VSC-based inverter. C_{dc} is the DC-link capacitor of the VSC. i_c and i_d are the capacitor current and the DC-side injected current of the converter, respectively. L_s and R_s are the inductance and the resistance of the phase reactor, respectively. i_s is the AC-side current of the VSC. u_c and u_s are the converter and the AC source voltage, respectively. The dynamics of the VSC-based inverter can be described as,

$$i_c = C_{dc}\frac{\mathrm{d}u_{dci}}{\mathrm{d}t}, \quad i_{dc} = i_c + i_d, \quad u_c - u_s = L_s\frac{\mathrm{d}i_s}{\mathrm{d}t} + R_s i_s \tag{3}$$

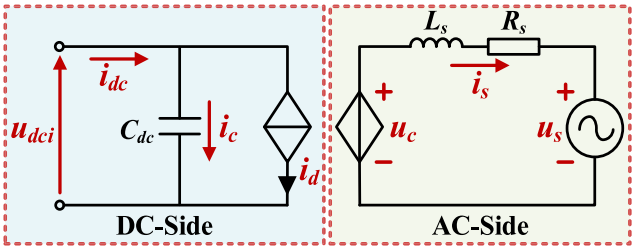

Fig. 4. Equivalent circuit of the VSC-based inverter.

The power balance equation holds when ignoring the loss of the converter,

$$P_c = u_{dci} i_d \approx u_c i_s \approx u_s i_s \tag{4}$$

To achieve the decoupling active and reactive power control, the classic vector control based on dq-coordinates is widely used in VSC-based converters. As shown in Fig. 5, the vector control comprises inner and outer loops. The inner current loop enables the AC output current to fast track its reference value.

$$u_c^d = K_{Pin}\left(i_s^{dref} - i_s^d\right) + K_{Iin}\int\left(i_s^{dref} - i_s^d\right)\mathrm{d}t + u_s^d - \omega_s L_s i_s^q \tag{5}$$

where K_{Pin} and K_{Iin} are the PI gains of the inner current control, respectively. The d- and q-axis components are represented by superscripts d and q, respectively, while the superscript ref denotes the reference value. Considering the d-axis components are closely associated with the active power of the converter, only the d-axis dynamic equation is presented in (5).

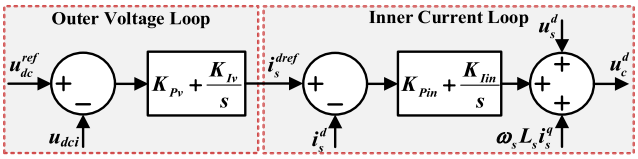

Fig. 5. Vector control of the VSC-based inverter.

The outer loop of the VSC-based inverter regulates the DC-link voltage and its control equations are expressed as,

$$i_s^{dref} = K_{Pv}\left(u_{dci} - u_{dc}^{ref}\right) + x_v, \quad x_v = K_{Iv}\int\left(u_{dci} - u_{dc}^{ref}\right)\mathrm{d}t \tag{6}$$

where K_{Pv} and K_{Iv} are the PI gains of the outer voltage loop. x_v is the integral part.

Analogous to the LCC, the dynamics of the PLL of the VSC-based inverter are also neglected when studying the DC-side stability of hybrid LCC-VSC HVDC systems [21–23].

(3) DC transmission line: To simplify the analysis, the classic RL line model is adopted in this paper. This is because the DC-side oscillation frequencies are within the feasible frequency range of the RL model. The dynamics of the DC transmission line are expressed as,

$$u_{dcr} - u_{dci} = L_{dc}\frac{\mathrm{d}i_{dc}}{\mathrm{d}t} + R_l i_{dc} \tag{7}$$

where L_{dc} is the DC transmission inductance and $L_{dc} = L_l + L_d + L_t$, in which L_l and R_l are the equivalent inductance and resistance of the DC transmission line.

2.3. Small-signal model of the hybrid HVDC link

Linearizing (4) around one equilibrium, it yields that,

$$\Delta P_c = u_{dci0}\Delta i_d + i_{d0}\Delta u_{dci} = 3u_s^d \Delta i_s^d/2 \Rightarrow \Delta i_d + g_0 \Delta u_{dci} = k_0 \Delta i_s^d, \quad g_0 = i_{d0}/u_{dci0}, \quad k_0 = 3u_s^d/2u_{dci0} \tag{8}$$

where Δ represents a generic small deviation from the equilibrium. The subscript 0 represents the initial steady-state value. u_s^d is the d-axis AC source voltage. g_0 and k_0 are the equivalent conductance and the concerning voltage coefficient of the VSC.

Combining (3) and (8), it provides that,

$$\frac{\mathrm{d}\Delta u_{dci}}{\mathrm{d}t} = \frac{g_0}{C_{dc}}\Delta u_{dci} - \frac{k_0}{C_{dc}}\Delta i_s^d + \frac{1}{C_{dc}}\Delta i_{dc} \tag{9}$$

As for the VSC's inner current loop, (10) holds by applying Laplace transformation on (3) and (5),

$$\left(sL_s + R_s + K_{Pin} + K_{Iin}/s\right)\Delta i_s^d = \left(K_{Pin} + K_{Iin}/s\right)\Delta i_s^{dref} \tag{10}$$

According to [24], the inner current dynamics are normally configured as first-order processes by choosing the PI gains as follows,

$$\Delta i_s^d = \Delta i_s^{dref}/\left(s\sigma_{in} + 1\right), \quad \left(L_s/K_{Pin} = R_s/K_{Iin} = \sigma_{in}\right) \tag{11}$$

The reference DC-link voltage is regarded as constant during normal operation. Based on (6) and (11), yields,

$$\frac{\mathrm{d}\Delta i_s^d}{\mathrm{d}t} = \frac{K_{Pv}}{\sigma_{in}}\Delta u_{dci} - \frac{1}{\sigma_{in}}\Delta i_s^d + \frac{1}{\sigma_{in}}\Delta x_v \tag{12}$$

(12) provides the linearized model of the VSC-based inverter. Similarly, the small-signal model of the LCC-based rectifier is obtained based on (1) and (2),

$$\Delta u_{dcr} = -\left(K_{Pc}V_o\sin\alpha_0 + d_\gamma\right)\Delta i_{dc} + V_o\sin\alpha_0\Delta x_c \tag{13}$$

Combining (7) and (13), it provides that,

$$\frac{\mathrm{d}\Delta i_{dc}}{\mathrm{d}t} = -\frac{1}{L_{dc}}\Delta u_{dci} - \frac{R_{eq0}}{L_{dc}}\Delta i_{dc} + \frac{V_o\sin\alpha_0}{L_{dc}}\Delta x_c \tag{14}$$

where R_{eq0} is the equivalent resistance of the HVDC transmission link and $R_{eq0} = R_l + d_\gamma + K_{Pc}V_o\sin\alpha_0$. Note that R_{eq0} also varies with the initial operating point.

Based on (2) and (6), the following equations hold,

$$\frac{\mathrm{d}\Delta x_v}{\mathrm{d}t} = K_{Iv}\Delta u_{dci}, \qquad \frac{\mathrm{d}\Delta x_c}{\mathrm{d}t} = -K_{Ic}\Delta i_{dc} \tag{15}$$

(9), (12), (14), and (15) constitute the small-signal model of the studied hybrid HVDC system, which is rewritten in a compact form as,

$$\Delta\dot{\mathbf{x}} = \mathbf{A}\Delta\mathbf{x}, \quad \Delta\mathbf{x} = \begin{bmatrix} \Delta u_{dci} \\ \Delta i_s^d \\ \Delta i_{dc} \\ \Delta x_v \\ \Delta x_c \end{bmatrix}, \quad \mathbf{A} = \left[\begin{array}{cc|ccc} g_0/C_{dc} & -k_0/C_{dc} & 1/C_{dc} & 0 & 0 \\ K_{Pv}/\sigma_{in} & -1/\sigma_{in} & 0 & 1/\sigma_{in} & 0 \\ \hline -1/L_{dc} & 0 & -R_{eq0}/L_{dc} & 0 & V_o\sin\alpha_0/L_{dc} \\ K_{Iv} & 0 & 0 & 0 & 0 \\ 0 & 0 & -K_{Ic} & 0 & 0 \end{array}\right] \tag{16}$$

2.4. Verification of the hybrid HVDC model

To verify the proposed model expressed by (16), a hybrid HVDC link is established in detail based on PSCAD/EMTDC. In the simulation, the converters adopt the full-switching model [25], while the DC transmission lines adopt the frequency-dependent model [26]. Table 1 presents the main parameters of the test system.

Fig. 6 compares the system dynamics with the detailed simulation model and those with the proposed model. Fig. 6(a), (c), and (e) show the dynamics of DC-link current, DC-link voltage, and d-axis current of the VSC under the sudden change of i_{dc}^{ref} from 2 kA to 1.6 kA, while Fig. 6(b), (d), and (e) show the system dynamics under the dip of u_{dc}^{ref} from 500 kV to 475 kV. It is observed from Fig. 6 that the step responses with the proposed model are aligned with those with the detailed simulation model under different DC-side perturbations, which verifies the accuracy of the proposed small-signal model of the LCC-VSC system.

Table 1. Main parameters of the test system.

Symbol	Item	Value
u_{dc}^{n}	Nominal DC-link voltage	500 kV
i_{dc}^{n}	Nominal DC-link current	2 kA
E	Nominal voltage of LCC-tied AC source	450 kV
ω_s	Nominal frequency of AC grids	50 Hz
d_γ	Equivalent commutation resistance	41 Ω
L_d	LCC-side smoothing reactor	200 mH
$(K_{Pc},\ K_{Ic})$	PI gains of constant current controller of LCC	(1, 100)
u_s	Nominal voltage of VSC-connected AC source	220 kV
C_{dc}	DC-link capacitance of VSC	100 μF
σ_{in}	Time constant of inner loop	4 ms
$(K_{Pv},\ K_{Iv})$	PI gains of DC voltage controller of VSC	(5, 125)
L_t	VSC-side supplementary reactor	50 mH
R_0	Resistance of DC line (per kilometer)	0.015 Ω
L_0	Inductance of DC line (per kilometer)	1.4 mH
l	DC line length	100 km

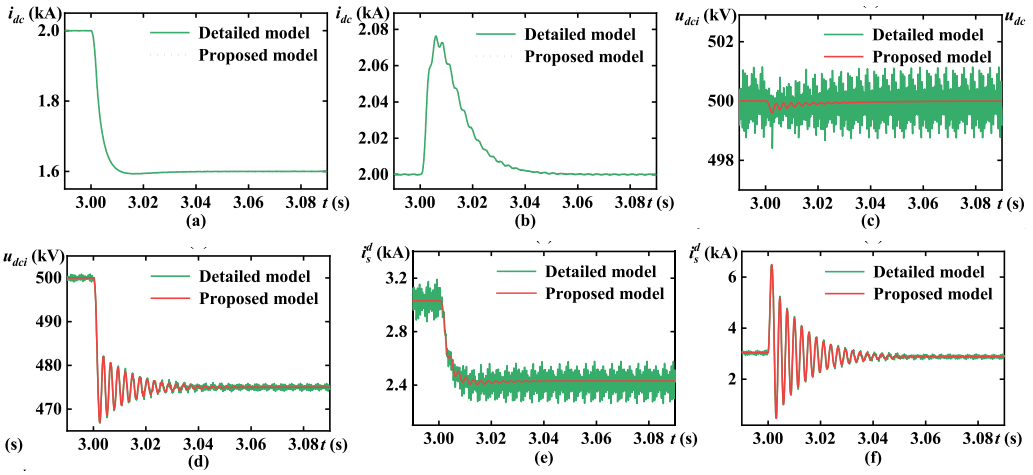

Fig. 6. Comparison between the detailed model and the proposed model: (a) DC current with the variation of i_{dc}^{ref} from 2 kA to 1.6 kA; (b) DC current with the variation of u_{dc}^{ref} from 500 kV to 475 kV; (c) DC voltage with the variation of i_{dc}^{ref} from 2 kA to 1.6 kA; (d) DC voltage with the variation of u_{dc}^{ref} from 500 kV to 475 kV; (e) d-axis component current with the variation of i_{dc}^{ref} from 2 kA to 1.6 kA; (f) d-axis component current with the variation of u_{dc}^{ref} from 500 kV to 475 kV.

3. Stability analysis of the hybrid HVDC link from DC-side perturbations

3.1. Dominant mode analysis

The small-signal stability discrimination of the studied hybrid HVDC system is achieved by examining the eigenvalues of the state matrix **A**, i.e., the system modes. The modes with small damping ratios dominate stability properties, which is known as the dominant modes. To find the influential factors on the dominant mode, the participation factor can be utilized. The participation factor of the kth state variable in the ith mode marked as p_{ki} is calculated as follows,

$$p_{ki} = v_{ki}u_{ki}/\mathbf{v}_i{}^{\mathrm{T}}\mathbf{u}_i \tag{17}$$

where $\mathbf{v}_i$ and $\mathbf{u}_i$ are the ith left eigenvector and right eigenvector of **A**, respectively. v_{ki} and u_{ki} are the kth element of $\mathbf{v}_i$ and $\mathbf{u}_i$, respectively.

Fig. 7 depicts the damping ratio and the participation factors of each mode. It is indicated that s_1 and s_2 have a much smaller damping ratio than other modes and thus are more influential to the system stability. In addition, it

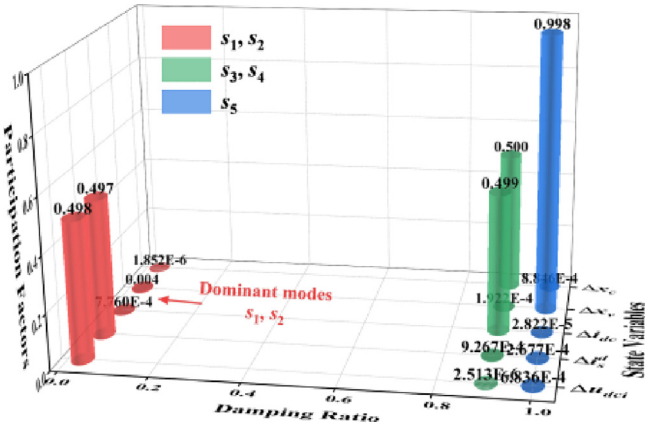

Fig. 7. Dominant mode analysis based on the state matrix.

is shown that the dominant mode (s_1 and s_2) is highly relevant to the DC-link voltage and the d-axis current of the VSC-based inverter.

By dividing the state variables into those with high and those with low participation in the dominant mode, (16) can be partitioned as,

$$\begin{bmatrix} \Delta\dot{\mathbf{x}}_1 \\ \Delta\dot{\mathbf{x}}_2 \end{bmatrix} = \begin{bmatrix} \mathbf{A_{11}} & \mathbf{A_{12}} \\ \mathbf{A_{21}} & \mathbf{A_{22}} \end{bmatrix} \begin{bmatrix} \Delta\mathbf{x}_1 \\ \Delta\mathbf{x}_2 \end{bmatrix}, \quad \Delta\mathbf{x_1} = \begin{bmatrix} \Delta u_{dci} & \Delta i_s^d \end{bmatrix}^{\mathrm{T}}, \quad \Delta\mathbf{x_2} = \begin{bmatrix} \Delta i_{dc} & \Delta x_v & \Delta x_c \end{bmatrix}^{\mathrm{T}} \tag{18}$$

where $\mathbf{A_{11}}$, $\mathbf{A_{12}}$, $\mathbf{A_{21}}$, and $\mathbf{A_{22}}$ are the partitioned matrices of $\mathbf{A}$ dividing at the second rows and columns.

Omitting the states less relevant to the dominant mode yields the characteristic equation of the truncated system,

$$F_d(s) = \det\left(s\mathbf{I_{11}} - \mathbf{A_{11}}\right) = s^2 + s\left(1/\sigma_{in} - g_0/C_{dc}\right) + \left(k_0 K_{Pv} - g_0\right)/\sigma_{in} C_{dc} \tag{19}$$

where $\mathbf{I_{11}}$ is the identity matrix of the same size as $\mathbf{A_{11}}$. Considering the small value of g_0 for HVDC converters, the dominant oscillation frequency of the studied system denoted by ω_d is obtained based on (19),

$$\omega_d = \sqrt{\left(k_0 K_{Pv} - g_0\right)/\sigma_{in} C_{dc}} \approx \sqrt{k_0 K_{Pv}/\sigma_{in} C_{dc}} \tag{20}$$

3.2. Dominant frequency model reduction

Due to the relatively high order of the state matrix, it is hard to directly derive the analytical stability criterion based on the classic modal analysis. To tackle that, a dominant frequency model reduction is proposed in this paper. By constructing a reduced-order model to approximate the system behaviors nearby the dominant oscillation frequency, the original state matrix can be significantly simplified without losing principal stability properties.

By applying Laplace transformation on (18), it provides that,

$$s\mathbf{I_{11}}\Delta\mathbf{x_1} = \mathbf{A_{11}}\Delta\mathbf{x_1} + \mathbf{A_{12}}\Delta\mathbf{x_2}, \quad s\mathbf{I_{22}}\Delta\mathbf{x_2} = \mathbf{A_{21}}\Delta\mathbf{x_1} + \mathbf{A_{22}}\Delta\mathbf{x_2} \tag{21}$$

where $\mathbf{I_{22}}$ is the identity matrix of the same size as $\mathbf{A_{22}}$. Combining the two equations in (21) yields,

$$s\mathbf{I_{11}}\Delta\mathbf{x_1} = \left(\mathbf{A_{11}} + \mathbf{A_{12}}\left(s\mathbf{I_{22}} - \mathbf{A_{22}}\right)^{-1}\mathbf{A_{21}}\right)\Delta\mathbf{x_1} \tag{22}$$

Based on (22), the characteristic equation of the original system can be written as,

$$F(s) = \det\left(\left(s\mathbf{I_{11}} - \mathbf{A_{11}}\right) - \mathbf{A_{12}}\left(s\mathbf{I_{22}} - \mathbf{A_{22}}\right)^{-1}\mathbf{A_{21}}\right) \tag{23}$$

In (23), the first term ($s\mathbf{I_{11}} - \mathbf{A_{11}}$) corresponds to the truncated system, while the second term ($\mathbf{A_{12}}(s\mathbf{I_{22}} - \mathbf{A_{22}})^{-1}\mathbf{A_{21}}$) reflects the effects of state variables less relevant to the dominant mode.

Considering the damping ratio of the dominant mode is rather small, the following equation holds nearby the dominant frequency,

$$s_{i_d} = \sigma_{i_d} + j\omega_{i_d} = \sqrt{{\sigma_{i_d}}^2 + {\omega_{i_d}}^2}\left(\sigma_{i_d}/\sqrt{\sigma_{i_d}^2 + \omega_{i_d}^2} + j\omega_{i_d}/\sqrt{\sigma_{i_d}^2 + \omega_{i_d}^2}\right) = \omega_d\left(-\zeta_d + j\sqrt{1-{\zeta_d}^2}\right) \approx j\omega_d \tag{24}$$

where s_{id} denotes the dominant mode. σ_{id} and ω_{id} are the real part and the imaginary part of s_{id}, respectively. ζ is the damping ratio of the dominant mode.

By substituting (24) into (23), the system characteristic equation is reduced in the neighborhood of the dominant frequency as,

$$\begin{aligned} F_r(s) &= \det\left(s\mathbf{I_{11}} - \mathbf{A_{11}} - \mathbf{A_{12}}\left(s\mathbf{I_{22}} - \mathbf{A_{22}}\right)^{-1}\mathbf{A_{21}}\right) = \det\left(s\mathbf{I_{11}} - \mathbf{A_{11}} - \mathbf{M_R} - j\mathbf{M_I}\right) \\ &\approx \det\left(s\mathbf{I_{11}} - \mathbf{A_{11}} - \mathbf{M_R} - s\mathbf{M_I}/\omega_d\right) = \det\left(s\left(\mathbf{I_{11}} - \mathbf{M_I}/\omega_d\right) - \left(\mathbf{A_{11}} + \mathbf{M_R}\right)\right) \end{aligned} \tag{25}$$

where $\mathbf{M_R}$ and $\mathbf{M_I}$ are supplementary matrices defined as,

$$\mathbf{M_R} = \mathrm{Re}\left\{\mathbf{A_{12}}\left(s\mathbf{I_{22}} - \mathbf{A_{22}}\right)^{-1}\mathbf{A_{21}}\right\}, \quad \mathbf{M_I} = \mathrm{Im}\left\{\mathbf{A_{12}}\left(s\mathbf{I_{22}} - \mathbf{A_{22}}\right)^{-1}\mathbf{A_{21}}\right\}$$

Based on (25), dynamics of the state variables less relevant to the dominant mode can be expressed by using two supplementary matrices with the same size of the truncated system. Since the reduced model approaches the original system model at the dominant frequency, the properties of the dominant mode can remain intact during the reduction.

3.3. Reduced model of the hybrid HVDC link

Based on the detailed expressions of $\mathbf{A_{12}}$, $\mathbf{A_{21}}$, and $\mathbf{A_{22}}$ provided by (16), the following equation holds,

$$\mathbf{A_{12}}\left(s\mathbf{I_{22}} - \mathbf{A_{22}}\right)^{-1}\mathbf{A_{21}} = \begin{bmatrix} -s/C_{dc}\left(s^2L_{dc} + sR_{eq0} + K_{Iv}V_o\sin\alpha_0\right) & 0 \\ K_{Iv}/s\sigma_{in} & 0 \end{bmatrix} \tag{26}$$

Based on (20) and (24), (26) is rewritten as follows nearby the dominant frequency,

$$\mathbf{A_{12}}\left(s\mathbf{I_{22}} - \mathbf{A_{22}}\right)^{-1}\mathbf{A_{21}}\big|_{s=j\omega_d} = \begin{bmatrix} \dfrac{-\sigma_{in}k_0K_{Pv}R_{eq0} + j\omega_d\sigma_{in}\left(k_0K_{Pv}L_{dc} - \sigma_{in}C_{dc}K_{Ic}V_o\sin\alpha_0\right)}{\left(k_0K_{Pv}L_{dc} - \sigma_{in}C_{dc}K_{Ic}V_o\sin\alpha_0\right)^2 + \sigma_{in}C_{dc}k_0K_{Pv}R_{eq0}^2} & 0 \\ -j\omega_dK_{Iv}C_{dc}/k_0K_{Pv} & 0 \end{bmatrix} \tag{27}$$

In HVDC transmission systems, the time constant of the VSC's inner loop is normally configured as several milliseconds, while the DC-link capacitor is several hundreds of μF. Because of the small values of σ_{in} and C_{dc}, (28) holds with typical hybrid HVDC parameters,

$$k_0K_{Pv}L_{dc} \gg \sigma_{in}C_{dc}K_{Ic}V_o\sin\alpha_0, \quad k_0K_{Pv}L_{dc}^2 \gg \sigma_{in}C_{dc}R_{eq0}^2 \tag{28}$$

Combining (27) and (28), the supplementary matrices $\mathbf{M_R}$ and $\mathbf{M_I}$ are reduced as,

$$\mathbf{M_R} = \begin{bmatrix} -\sigma_{in}R_{eq0}/k_0K_{Pv}L_{dc}^2 & 0 \\ 0 & 0 \end{bmatrix}, \quad \mathbf{M_I} = \omega_d\begin{bmatrix} \sigma_{in}/k_0K_{Pv}L_{dc} & 0 \\ -K_{Iv}C_{dc}/k_0K_{Pv} & 0 \end{bmatrix} \tag{29}$$

By inserting (29) into (25), the reduced characteristic equation of the hybrid HVDC link is obtained as,

$$\begin{aligned} &F_r(s) = \det\left(s\mathbf{I_{11}} - \mathbf{A_{11}} - \mathbf{M_R} - s\mathbf{M_I}/\omega_d\right) = a_2s^2 + a_1s + a_0, \\ &a_2 = 1 - \frac{\sigma_{in}}{k_0K_{Pv}L_{dc}}, \quad a_1 = \frac{1}{\sigma_{in}} - \frac{g_0}{C_{dc}} - \frac{K_{Iv}}{K_{Pv}} - \frac{1}{k_0K_{Pv}L_{dc}} + \frac{\sigma_{in}R_{eq0}}{k_0K_{Pv}L_{dc}^2}, \\ &a_0 = \frac{k_0K_{Pv} - g_0}{\sigma_{in}C_{dc}} + \frac{R_{eq0}}{k_0K_{Pv}L_{dc}^2}. \end{aligned} \tag{30}$$

3.4. Stabilizing conditions

Due to the small values of σ_{in} and g_0, the following inequalities hold with practical HVDC engineering parameters,

$$a_2 = 1 - \frac{\sigma_{in}}{k_0K_{Pv}L_{dc}} = \frac{k_0K_{Pv}L_{dc} - \sigma_{in}}{k_0K_{Pv}L_{dc}} > 0, \qquad a_0 = \frac{k_0K_{Pv} - g_0}{\sigma_{in}C_{dc}} + \frac{R_{eq0}}{k_0K_{Pv}L_{dc}^2} \approx \frac{k_0K_{Pv}}{\sigma_{in}C_{dc}} + \frac{R_{eq0}}{k_0K_{Pv}L_{dc}^2} > 0 \tag{31}$$

Since a_2 and a_0 are always positive, the sign of a_1 determines the stability. Based on (30), the stability criterion for the hybrid HVDC link is expressed as,

$$a_1 = 1/\sigma_{in} - g_0/C_{dc} - K_{Iv}/K_{Pv} - 1/k_0 K_{Pv} L_{dc} + \sigma_{in} R_{eq0}/k_0 K_{Pv} L_{dc}^2 > 0 \tag{32}$$

(32) indicates that enlarging the integral gain of the DC voltage controller or downsizing the DC-link capacitor of the VSC will degrade the system stability. To quantify the influences of system parameters on the stability of the hybrid HVDC link, the stability margin marked as S is defined as,

$$\begin{aligned} S &= \frac{1}{\sigma_{in}} - \frac{g_0}{C_{dc}} - \frac{K_{Iv}}{K_{Pv}} - \frac{1}{k_0 K_{Pv} L_{dc}} + \frac{\sigma_{in} R_{eq0}}{k_0 K_{Pv} L_{dc}^2} \\ &= \frac{1}{\sigma_{in}} - \frac{i_{dc0}}{C_{dc} u_{dci0}} - \frac{K_{Iv}}{K_{Pv}} - \frac{2u_{dci0}}{3K_{Pv} L_{dc} u_s^d} + \frac{2\sigma_{in} u_{dci0} r\left(u_{dci0}, i_{dc0}\right)}{3K_{Pv} L_{dc}^2 u_s^d}, \\ r\left(u_{dci0}, i_{dc0}\right) &= R_l + d_\gamma + K_{Pc} V^+, \quad V^+ = \sqrt{V_o^2 - \left(u_{dci0} + \left(R_l + d_\gamma\right) i_{dc0}\right)^2}. \end{aligned} \tag{33}$$

(32) and (33) indicate that the hybrid HVDC system is stable if $S > 0$ and the system reaches the stability boundary if $S = 0$. Taking the partial derivatives of S with respect to u_{dci0} and i_{dc0}, yields,

$$\begin{aligned} \frac{\partial S}{\partial u_{dci0}} &= \frac{i_{dc0}}{C_{dc} u_{dci0}^2} - \frac{2}{3K_{Pv} L_{dc} u_s^d} + \frac{2\sigma_{in} K_{Pc} V_o u_{dci0}}{3K_{Pv} L_{dc}^2 u_s^d V^+} > 0 \\ \frac{\partial S}{\partial i_{dc0}} &= -\frac{1}{C_{dc} u_{dci0}} - \frac{2\sigma_{in} K_{Pc}\left(R_l + d_\gamma\right) u_{dci0}\left(u_{dci0} + \left(R_l + d_\gamma\right) i_{dc0}\right)}{3K_{Pv} L_{dc}^2 u_s^d V^+} < 0 \end{aligned} \tag{34}$$

Note that the first relation in (34) holds because C_{dc} is fairly small with typical HVDC parameters such that the first term is larger than the second term of the right side. (34) manifests that reduced DC voltage operation or a heavy load will deteriorate the DC-side stability of the hybrid HVDC transmission system.

The impacts of controller parameters on the DC-side stability are obtained similarly,

$$\begin{aligned} \frac{\partial S}{\partial K_{Pc}} &= \frac{2\sigma_{in} u_{dci0} V^+}{3K_{Pv} L_{dc}^2 u_s^d} > 0, \\ \frac{\partial S}{\partial K_{Pv}} &= \frac{1}{K_{Pv}^2}\left(K_{Iv} + \frac{2u_{dci0}}{3L_{dc} u_s^d} - \frac{2\sigma_{in} u_{dci0} R_{eq0}}{3L_{dc}^2 u_s^d}\right) > 0, \\ \frac{\partial S}{\partial \sigma_{in}} &= -\left(\frac{1}{\sigma_{in}^2} - \frac{2R_{eq0} u_{dci0}}{3K_{Pv} L_{dc}^2 u_s^d}\right) < 0 \end{aligned} \tag{35}$$

It is concluded from (35) that declining the proportional gain of the constant current controller and that of the DC voltage controller or enlarging the time constant of the inner loop of the VSC may jeopardize the system stability as well.

In order to build up clear and concise relationships between system parameters and stability, simplified stabilizing conditions for hybrid HVDC links are derived as follows.

Based on (34), a sufficient condition of (32) can be constructed as,

$$S \geq S\left(u_{dc}^{\min}, i_{dc}^{\max}\right) > 1/\sigma_{in} - i_{dc}^{\max}/C_{dc} u_{dc}^{\min} - K_{Iv}/K_{Pv} - 2u_{dc}^{\min}/3K_{Pv} L_{dc} u_s^d > 0 \tag{36}$$

where $i_{dc}^{\max}$ and $u_{dc}^{\min}$ are the allowable maximum current and the minimum voltage of the HVDC transmission system.

Rearranging (36), it provides that,

$$K_{Iv} < \left(1/\sigma_{in} - i_{dc}^{\max}/C_{dc} u_{dc}^{\min}\right) K_{Pv} - 2u_{dc}^{\min}/3L_{dc} u_s^d \tag{37}$$

Considering the integral gain K_{Iv} should be positive, the following inequalities are obtained based on (37),

$$\begin{aligned} &K_{Pv} > 2\sigma_{in} C_{dc}\left(u_{dc}^{\min}\right)^2 / 3L_{dc} u_s^d \left(C_{dc} u_{dc}^{\min} - \sigma_{in} i_{dc}^{\max}\right), \\ &0 < K_{Iv} < \left(1/\sigma_{in} - i_{dc}^{\max}/C_{dc} u_{dc}^{\min}\right) K_{Pv} - 2u_{dc}^{\min}/3L_{dc} u_s^d \end{aligned} \tag{38}$$

(38) provides simplified stabilizing conditions for hybrid HVDC links. Given the key parameters of a specified system, it is convenient to design the DC voltage controller parameters as per (38) to guarantee the DC-side stability of the system.

4. Case studies

The accuracy of dominant frequency model reduction is verified by the classic eigen analysis. Besides, nonlinear simulations based on PSCAD/EMTDC are carried out to verify the relationship between the system stability and key parameters. The schematic and main parameters of the test system can refer to in Fig. 1 and Table 1, respectively.

4.1. Verification of dominant frequency model reduction

Fig. 8 compares the system eigenvalues with the proposed and the reduced model. Fig. 8(a) and (b) show the influences of operating points on the eigenvalues. Fig. 8(a) shows that declining the DC-link voltage will cause the dominant eigenvalues (s_1 and s_2) to move towards the left-hand plane (LHP) and close to the real axis, implying the oscillations will be less damped with lower frequencies. In contrast, Fig. 8(b) indicates that decreasing the transmitted DC current will enhance the system damping but slightly impact the oscillation frequency. Therefore, DC-side instability is more likely to occur in hybrid HVDC links under reduced DC voltage operation with a heavy load. Fig. 8(c) and (d) illustrate the changes of the eigenvalues with various parameters of physical systems, which shows that the DC-link capacitance mainly affects the dominant mode, while the inductance of the transmission line mainly influences other nondominant modes. As illustrated by Fig. 8(c), downsizing the capacitor of the VSC will jeopardize the system stability and increase the oscillation frequency. Fig. 8(e) to (h) present the influences of control parameters on the DC-side stability. Fig. 8(e) shows that increasing the proportional gain of the LCC's constant current controller slightly improves the system dynamic properties. In contrast, Fig. 8(f) shows that the increase of the time constant of the VSC's inner control loop significantly deteriorates stability properties and slows down the oscillation frequency. As for the VSC's outer voltage loop, Fig. 8(g) shows that enlarging the proportional gain will lead to the increase of the dominant mode's damping ratio and its natural oscillation frequency. However, as shown in Fig. 8(h), elevating the integral gain of the VSC's outer loop will sharply reduce the system damping and slightly affect the oscillation frequency.

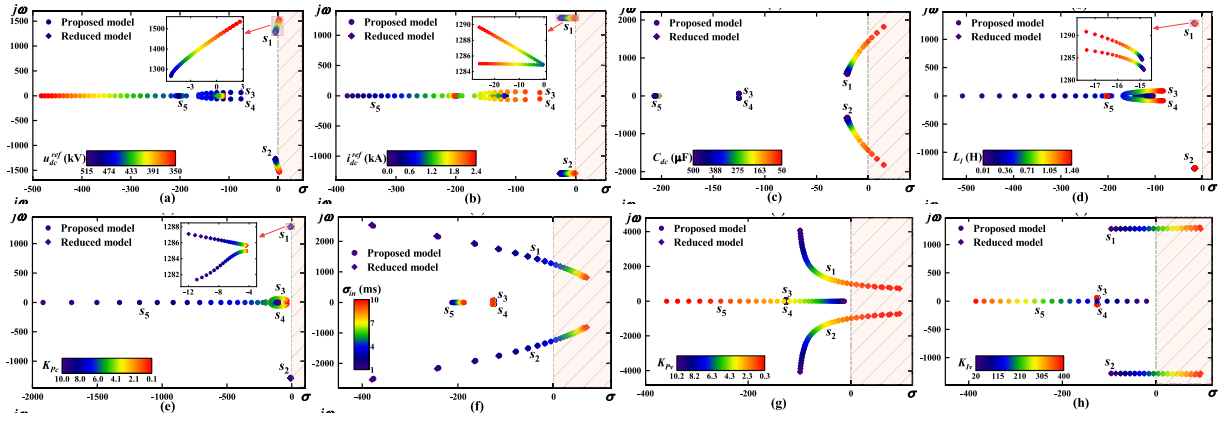

Fig. 8. Impacts of system parameters on the eigenvalues of the state matrix: (a) u_{dc}^{ref} from 515 kV to 350 kV; (b) i_{dc}^{ref} from 0 to 2.4 kA; (c) C_{dc} from 500 μF to 50 μF; (d) L_l from 0.01 H to 1.4 H; (e) K_{Pc} from 10 to 0.1; (f) σ_{in} from 1 ms to 10 ms; (g) K_{Pv} from 10.2 to 0.3; (h) K_{Iv} from 20 to 400.

To sum up, the DC-side stability of hybrid HVDC links will deteriorate with reduced DC voltage operation, a heavy load, a small DC-link capacitor, slow VSC's inner dynamics, a low proportional and a large integral gain of the outer voltage loop, which is in line with (34) and (35). It is also observed in Fig. 8 that the dominant eigenvalues calculated by the proposed model (denoted by circular points) are fairly close to those with the reduced model

(denoted by diamond points) under various system parameters, demonstrating the accuracy of dominant frequency model reduction.

Fig. 9 shows the influences of the PI gains of the VSC's outer voltage loop on the system damping, where the blue region denotes positive damping, while the red region denotes negative damping. The damping will be enlarged by increasing the proportional gain or decreasing the integral gain. The stability boundary of the system is obtained by connecting the points corresponding to zero damping together, which is denoted by the yellow solid line in Fig. 9. Based on (33), the stability boundary with the reduced model is the curve corresponding to $S = 0$, which is denoted by the purple dash line in Fig. 9. It is observed that the stability boundary with the proposed and the reduced models are almost the same, which verifies the accuracy of the derived stability criterion expressed by (32). Moreover, by taking the mark of equality of (37), another stability boundary based on the simplified sufficient stabilizing condition can be obtained, denoted by the brown dash–dot line in Fig. 9. Note that the boundary locates in the blue region that corresponds to positive damping, indicating the conservatism of the stabilizing conditions expressed by (37) and (38).

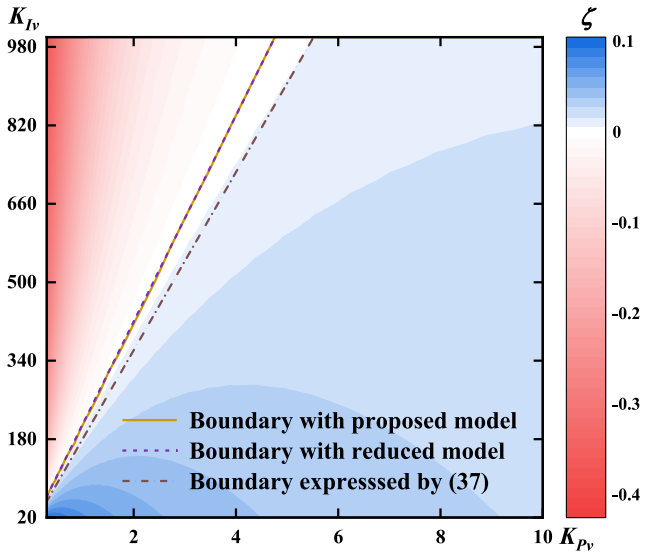

Fig. 9. Stability boundary with different models.. (For interpretation of the references to color in this figure legend, the reader is referred to the web version of this article.)

4.2. Nonlinear simulation analysis

Fig. 10 shows the nonlinear simulation results under sudden DC voltage dips with various system parameters. Fig. 10(a) depicts the system dynamics under different voltage dips. When the DC-link voltage becomes lower, the hybrid HVDC system gradually exhibits less damped oscillations. Divergent oscillations occur when the DC-link voltage dips to 350 kV. Besides, the oscillation frequency becomes larger as the DC-link voltage decreases. Fig. 10(b) indicates that increasing the transmitted current is detrimental to suppressing the DC-link oscillations. The system is destabilized when the DC-link current increases to 2.4 kA. Also, it is indicated by Fig. 10(b) that the change of the DC-link current has negligible influences to the oscillation frequency. Fig. 10(c) presents the system dynamics with different DC-link capacitances, which clearly shows that decreasing the DC-link capacitance significantly augments and accelerates the DC-side oscillations. This can be explained by the fact that a smaller capacitor possesses less capacity for storing the transient energy during DC-side perturbations. As illustrated by Fig. 10(d), the system damping and the oscillation frequency will decrease when slowing down the VSC's inner dynamics. Consequently, a small time constant of the VSC's inner loop is recommended for hybrid HVDC links not only to fast track the reference current but also to suppress DC-link resonances. Fig. 10(e) depicts that declining the proportional gain of the VSC's outer voltage loop will sharply weaken the damping and reduce the oscillation

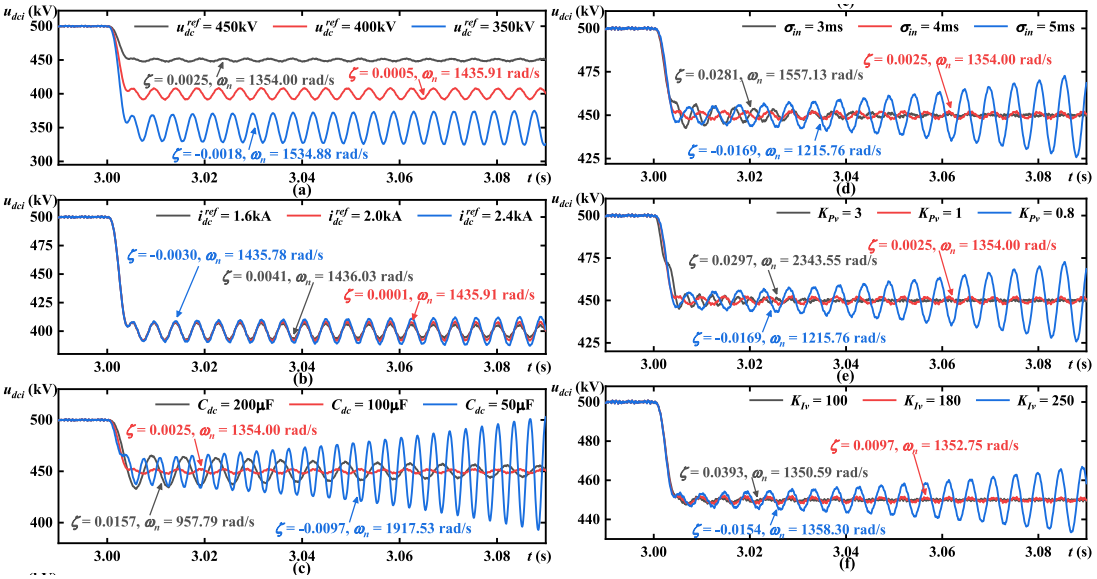

Fig. 10. Impacts of system parameters on system dynamics: (a) under different voltage dips; (b) under different loads; (c) with different DC-link capacitances; (d) with different time constant of the VSC's inner loop; (e) with different proportional gains of the DC voltage control; (f) with different integral gains of the DC voltage control.

frequency. In contrast, the change of the integral gain of the VSC's outer loop rarely affects the oscillation frequency as depicted in Fig. 10(f). It is also shown in Fig. 10(f) that the system exhibits apparent divergent oscillations with an integral gain of 250. However, DC-link oscillations are significantly damped when the integral gain is below 180, which equals the right side of the inequality expressed by (37). The simulation results indicate that the DC-link stability of hybrid HVDC systems can be ensured, provided that the simplified stabilizing conditions expressed by (38) can be satisfied. Additionally, it is worth mentioning that in Fig. 10, the damping ratios and natural oscillation frequencies calculated based on the proposed model perfectly coincide with the simulation results. The nonlinear simulations effectively verify the stability analysis results of hybrid HVDC links.

5. Conclusion

Analytical DC-side stabilizing conditions for hybrid HVDC links are explored in this paper. A reduced-order model capable of accurately describing the hybrid HVDC system behaviors in the neighborhood of the dominant oscillation frequency is first obtained based on dominant frequency model reduction. Subsequently, an analytical stability criterion for the system is derived, which indicates that reduced DC voltage operation, a heavy load, a small DC-link capacitor, a slow time constant of VSC's inner loop, a small proportional and a large integral gain of VSC's outer voltage loop will deteriorate the DC-side stability of hybrid HVDC links. Accordingly, the region of DC voltage regulator parameters for guaranteeing the system stability under DC-side perturbations can be determined.

Declaration of competing interest

The authors declare that they have no known competing financial interests or personal relationships that could have appeared to influence the work reported in this paper.

Data availability

No data was used for the research described in the article.

Acknowledgments

This project is supported by National Key Research and Development Program of China (2022YFB2402701).

References

[1] Cardesin J, Alonso J, Lopez-Corominas E, Calleja A, Ribas J, Rico-Secades M, et al. Small-signal analysis of a low-cost power control for LCC series-parallel inverters with resonant current mode control for hid lamps. IEEE Trans Power Electron 2005;20(5):1205–12. http://dx.doi.org/10.1109/TPEL.2005.854066.

[2] Zhang F, Xin H, Wu D, Wang Z, Gan D. Assessing strength of multiinfeed LCC–HVDC systems using generalized short-circuit ratio. IEEE Trans Power Syst 2019;34(1):467–80. http://dx.doi.org/10.1109/TPWRS.2018.2868958.

[3] Xu L, Xin H, Huang L, Yuan H, Ju P, Wu D. Symmetric admittance modeling for stability analysis of grid-connected converters. IEEE Trans Energy Convers 2020;35(1):434–44. http://dx.doi.org/10.1109/TEC.2019.2943255.

[4] Zhao Z. HVDC applications of GTO voltage source inverters. 1993.

[5] Zhang Z, Xu Z, Xue Y, Tang G. DC-side harmonic currents calculation and DC-loop resonance analysis for an LCC–MMC hybrid HVDC transmission system. IEEE Trans Power Deliv 2015;30(2):642–51. http://dx.doi.org/10.1109/TPWRD.2013.2297442.

[6] Torres-Olguin RE, Garces A, Molinas M, Undeland T. Integration of onshore wind farm using a hybrid HVDC transmission composed by the pwm current-source converter and line-commutated converter. IEEE Trans Energy Convers 2013;28(1):125–34. http://dx.doi.org/10.1109/TEC.2012.2230535.

[7] Haleem NM, Rajapakse AD, Gole AM, Fernando IT. Investigation of fault ride-through capability of hybrid VSC–LCC multi-terminal HVDC transmission systems. IEEE Trans Power Deliv 2019;34(1):241–50. http://dx.doi.org/10.1109/TPWRD.2018.2868467.

[8] Kaur J, Chaudhuri NR. A coordinating control for hybrid HVDC systems in weak grid. IEEE Trans Ind Electron 2019;66(11):8284–95. http://dx.doi.org/10.1109/TIE.2018.2890496.

[9] Lee G-S, Kwon D-H, Moon S-I. DC current and voltage droop control method of hybrid HVDC systems for an on shore wind farm connection to enhance AC voltage stability. IEEE Trans Energy Convers 2021;36(1):468–79. http://dx.doi.org/10.1109/TEC.2020.3005777.

[10] Chen X, Li H, Wang G, Xu C, Liang Y. A convolution power-based protection scheme for hybrid multiterminal HVDC transmission systems. IEEE J. Emerg. Sel. Top. Power Electron. 2021;9(2):1655–67. http://dx.doi.org/10.1109/JESTPE.2020.2978262.

[11] Liang Y, Jiang L, Li H, Wang G, Zhong Q, Wang L. Fault analysis and traveling wave protection based on phase characteristics for hybrid multiterminal HVDC systems. IEEE J. Emerg. Sel. Top. Power Electron. 2021;1. http://dx.doi.org/10.1109/JESTPE.2021.3102958.

[12] Guo C, Yin Z, Zhao C, Iravani R. Small-signal dynamics of hybrid LCC–VSC HVDC systems. Int J Electr Power Energy Syst 2018;98:362–72.

[13] Zhu J, Li S, Yu L, Bu S, Li Y, Wang Y, et al. Coherence analysis of system characteristics and control parameters for hybrid HVDC transmission systems based on small-signal modeling. IEEE J. Emerg. Sel. Top. Power Electron. 2021;9(6):7436–46. http://dx.doi.org/10.1109/JESTPE.2020.3014434.

[14] Li B, Liang Y, Wang G, Li H, Chen X. A control parameter design method for hybrid multi-terminal HVDC system. IEEE Access 2020;8:18669–80. http://dx.doi.org/10.1109/ACCESS.2020.2967835.

[15] Kokotovic PV, Allemong JJ, Winkelman JR, Chow JH. Singular perturbation and iterative separation of time scales. Automatica 1980;16(1):23–33.

[16] Castro R, Ferreira de Jesus J. A wind park reduced-order model using singular perturbations theory. IEEE Trans Energy Convers 1996;11(4):735–41. http://dx.doi.org/10.1109/60.556372.

[17] Perez-arriaga IJ, Verghese GC, Schweppe FC. Selective modal analysis with applications to electric power systems, part I: Heuristic introduction. IEEE Transactions on Power Apparatus and Systems PAS- 1982;101(9):3117–25. http://dx.doi.org/10.1109/TPAS.1982.317524.

[18] Pulgar-Painemal HA, Sauer PW. Reduced-order model of type-C wind turbine generators. Electr Power Syst Res 2011;81(4):840–5.

[19] Ali HR, Kunjumuhammed LP, Pal BC, Adamczyk AG, Vershinin K. Model order reduction of wind farms: Linear approach. IEEE Trans Sustain Energy 2019;10(3):1194–205. http://dx.doi.org/10.1109/TSTE.2018.2863569.

[20] Hao Q, Li Z, Gao F, Zhang J. Reduced-order small-signal models of modular multilevel converter and MMC-based HVDC grid. IEEE Trans Ind Electron 2019;66(3):2257–68. http://dx.doi.org/10.1109/TIE.2018.2869358.

[21] Stamatiou G, Bongiorno M. Stability analysis of two-terminal VSC–HVDC systems using the net-damping criterion. IEEE Trans Power Deliv 2016;31(4):1748–56. http://dx.doi.org/10.1109/TPWRD.2016.2516987.

[22] Xu L, Fan L, Miao Z. DC impedance-model-based resonance analysis of a VSC–HVDC system. IEEE Trans Power Deliv 2015;30(3):1221–30. http://dx.doi.org/10.1109/TPWRD.2014.2367123.

[23] Li Y, Li J, Xiao H, Zhang J, Du Z. Stability analysis of droop-based converter using siso method from DC side perturbation. IEEE Trans Power Deliv 2020;1. http://dx.doi.org/10.1109/TPWRD.2020.3034282.

[24] Yazdani A, Iravani R. Voltage-sourced converters in power systems: Modeling, control, and applications. John Wiley & Sons; 2010.

[25] Sybille G, Le-Huy H, Gagnon R, Brunelle P. Analysis and implementation of an interpolation algorithm for fixed time-step digital simulation of PWM converters. In: 2007 IEEE international symposium on industrial electronics. 2007, p. 793–8. http://dx.doi.org/10.1109/ISIE.2007.4374698.

[26] Castellanos F, Marti J. Full frequency-dependent phase-domain transmission line model. IEEE Trans Power Syst 1997;12(3):1331–9. http://dx.doi.org/10.1109/59.630478.